

Article

Strain and Deformation Analysis Using 3D Geological Finite Element Modeling with Comparison to Extensometer and Tiltmeter Observations

Meng Li ^{1,2,3,*} , Hexiong Lu ^{1,3,4}, Ahmed El-Mowafy ² , Tieding Lu ^{1,2,3} and Aiping Zhao ⁵

¹ Key Laboratory of Mine Environmental Monitoring and Improving around Poyang Lake, Ministry of Natural Resources, East China University of Technology, Nanchang 330013, China; 2021120341@ecut.edu.cn (H.L.); tdlu@ecut.edu.cn (T.L.)

² School of Earth and Planetary Sciences, Curtin University, GPO Box U1987, Perth, WA 6845, Australia; a.el-mowafy@curtin.edu.au

³ School of Surveying and Geoinformation Engineering, East China University of Technology, Nanchang 330013, China

⁴ Jiangxi Spatial Geographic Information Engineering Group Co., Ltd., Nanchang 330013, China

⁵ Engineering Research Center for Seismic Disaster Prevention and Engineering Geological Disaster Detection of Jiangxi Province, Nanchang 330013, China

* Correspondence: limeng1986@ecut.edu.cn

Abstract: This study verifies the practicality of using finite element analysis for strain and deformation analysis in regions with sparse GNSS stations. A digital 3D terrain model is constructed using DEM data, and regional rock mass properties are integrated to simulate geological structures, resulting in the development of a 3D geological finite element model (FEM) using the ANSYS Workbench module. Gravity load and thermal constraints are applied to derive directional strain and deformation solutions, and the model results are compared to actual strain and tilt measurements from the Jiujiang Seismic Station (JSS). The results show that temperature variations significantly affect strain and deformation, particularly due to the elevation difference between the mountain base and summit. Higher temperatures increase thermal strain, causing tensile effects, while lower temperatures reduce thermal strain, leading to compressive effects. Strain and deformation patterns are strongly influenced by geological structures, gravity, and topography, with valleys experiencing tensile strain and ridges undergoing compression. The deformation trend indicates a southwestward movement across the study area. A comparison of FEM results with ten years of strain and tiltmeter data from JSS reveals a strong correlation between the model predictions and actual measurements, with correlation coefficients of 0.6 and 0.75 for strain in the NS and EW directions, and 0.8 and 0.9 for deformation in the NS and EW directions, respectively. These findings confirm that the 3D geological FEM is applicable for regional strain and deformation analysis, providing a feasible alternative in areas with limited GNSS monitoring. This method provides valuable insights into crustal deformation in regions with sparse strain and deformation measurement data.

Keywords: finite element analysis; three-dimensional geological modeling; strain; deformation; tilt; feasibility



Citation: Li, M.; Lu, H.; El-Mowafy, A.; Lu, T.; Zhao, A. Strain and Deformation Analysis Using 3D Geological Finite Element Modeling with Comparison to Extensometer and Tiltmeter Observations. *Remote Sens.* **2024**, *16*, 3967. <https://doi.org/10.3390/rs16213967>

Academic Editors: Tomaž Podobnikar, Thomas Oommen and Mirko Francioni

Received: 2 September 2024

Revised: 3 October 2024

Accepted: 18 October 2024

Published: 25 October 2024



Copyright: © 2024 by the authors. Licensee MDPI, Basel, Switzerland. This article is an open access article distributed under the terms and conditions of the Creative Commons Attribution (CC BY) license (<https://creativecommons.org/licenses/by/4.0/>).

1. Introduction

Strain and deformation hold significant importance in geoscience and engineering, particularly in crustal dynamics, geological hazard monitoring, and infrastructure protection [1,2]. Understanding strain and deformation not only reveal the dynamic processes within the Earth's crust but also provide scientific foundations for early warning of natural disasters, thereby helping to mitigate potential risks [3–5]. The Global Navigation Satellite System (GNSS) has become a crucial tool for monitoring crustal deformation [6,7]. By precisely measuring the spatial positional changes of surface points, GNSS technology can

provide high-precision data on crustal deformation, making it widely applicable in the field of strain and deformation monitoring [8,9]. However, the distribution of GNSS monitoring stations is uneven. This is especially true in regions with complex geographical conditions or relatively underdeveloped economies, where the sparsity of GNSS stations results in inadequate spatial resolution of the monitoring data, thereby limiting the effectiveness of strain and deformation monitoring. Therefore, in areas where GNSS data is very limited and sparsely distributed, finite element numerical simulation technology is introduced to estimate regional strain and deformation [10–13].

Finite element numerical simulation technology is playing an increasingly important role in the study of regional stress, strain, and seismic activity [14]. For example, a two-dimensional (2D) vertical plane strain finite element model (FEM) has been used to simulate the deformation of the Tianshan orogenic belt as well as changes in the displacement and stress fields of the fault system [10]. The finite element method, combined with an elastic 2D plane stress model, has been used to simulate the current and Miocene maximum horizontal compressive stress direction and magnitude of the Indo-Australian plate [11]. In the Indian subcontinent, where in-situ stress measurements are limited, FEM has been applied to simulate the direction and magnitude of stress, providing constraints on the intraplate stress field in that region [12]. In the Zagros–Iranian Plateau region, finite element numerical simulation has been used to study tectonic stress and deformation, with the results contributing to seismic hazard assessments [13]. FEM has also been used to reconstruct and simulate the stress within blocks surrounding tilted fractures in fault damage zones [15]. Dynamic finite element analysis has been applied to simulate normal fault earthquakes, assessing uncertainties related to empirical relationships for estimating earthquake magnitude [16]. By establishing a 2D FEM of the Lushan earthquake and its surrounding area, researchers explored factors such as eastward extrusion from the Tibetan Plateau, regional topography, and the rupture characteristics of the Lushan earthquake [17]. There are also studies that perform stress analysis on a standard three-dimensional (3D) finite element topographic model for East Azerbaijan Province, Iran [18]. Based on the latest crustal structure data, a 3D FEM was established for the Anninghe–Zemuhe–Xiaojiang fault zone to analyze the tectonic and Coulomb stresses caused by fault rupture and their relationship with historical major earthquakes [19]. These case studies demonstrate that in regions where in situ stress and GNSS data are very limited and sparsely distributed, finite element numerical simulation has become an alternative method for analyzing regional stress, strain, and deformation.

As a case example, in Jiangxi Province, China, the GNSS physical deformation monitoring network consists of five GNSS stations (Figure 1a), leading to inadequate coverage of terrain deformation monitoring. To address this challenge, fixed-point deformation monitoring stations have been established at seismic stations to facilitate short-term regional seismic activity tracking and analysis (Figure 1a). Among them, the Jiujiang seismic station (JSS) (Figure 1b), situated at the highest elevation in Jiangxi Province, began collecting digital geophysical strain observation data in 2007 and has since gradually accumulated a substantial dataset on terrain deformation. These data provide a valuable foundation for further research and for addressing the gaps in deformation monitoring coverage. The JSS, situated at the foothills on the northwest side of Lushan Mountain in Jiujiang City, is at an elevation of 110 m (latitude 29.65°N, longitude 116.01°E). The surrounding topography is characterized by a kidney-shaped mountain formation, representing a NE–SW-oriented folded fault block mountain. Within the weather observation housing at the station, temperature fluctuations are minimal, and the bedrock is composed of siliceous limestone. The station is equipped with a range of terrain deformation observation instruments, including vertical pendulum tiltmeters and extensometers, among other technologies. Over several years, the station has collected an extensive dataset, consistently maintaining high-quality observational data. In this contribution, and by using the JSS as a case study, the integration of actual geological structure data facilitates the analysis of strain and deformation based on 3D geological FEM.

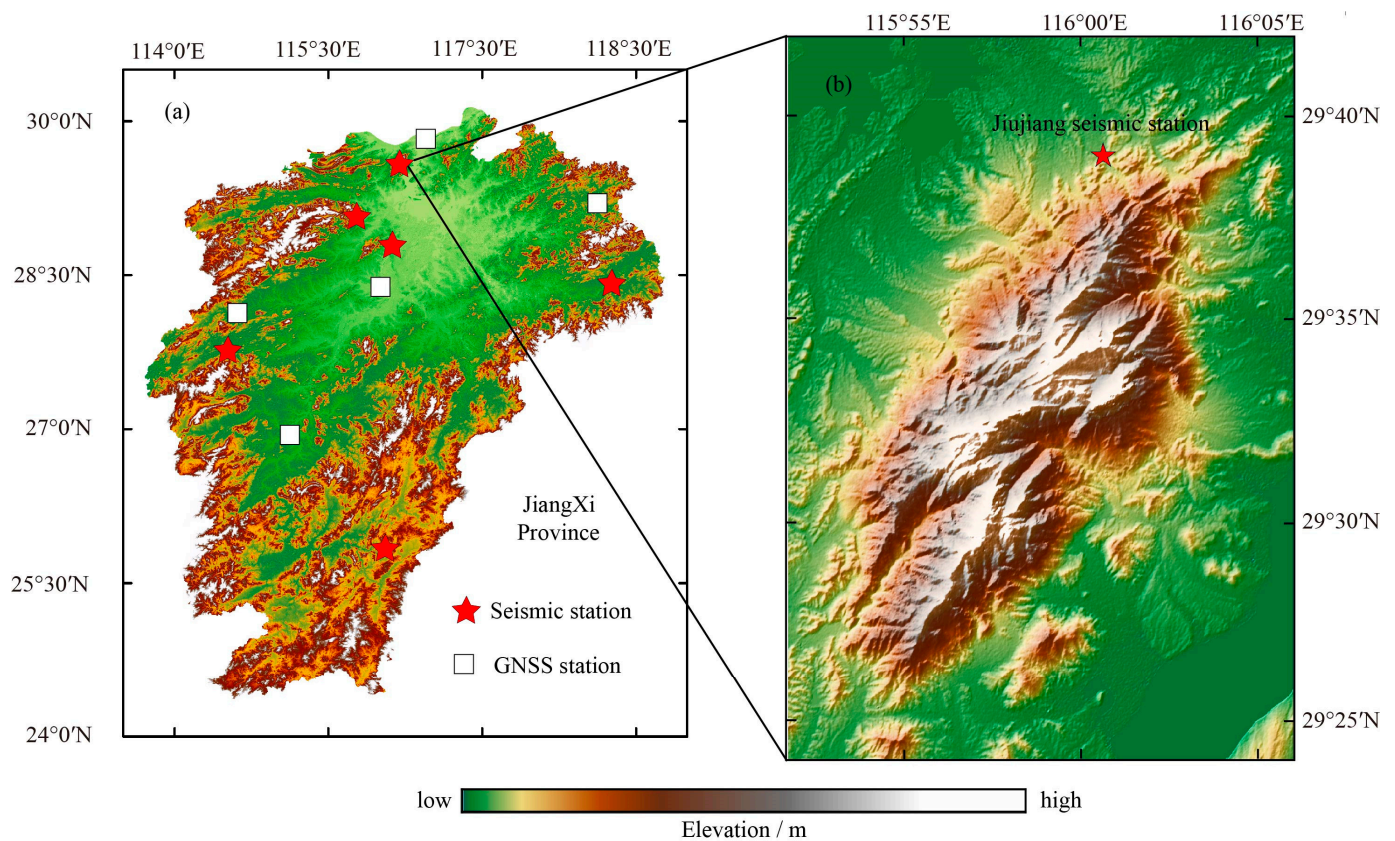


Figure 1. (a) The distribution map of geophysical observation stations in Jiangxi Province, China, with red pentagrams representing seismic deformation stations and white squares representing GNSS observation stations. (b) Topography of the Jiujiang seismic station (JSS), with red pentagrams representing JSS. In (a,b), the colors represent elevation, with green indicating plains and brown representing mountainous areas.

The 3D geological FEM is constructed using the finite element analysis software ANSYS (version 16.0, dated 22 October 2023). ANSYS enables the creation of high-precision 3D geological models, improving the efficiency of complex geometric modeling and ensuring the accuracy of finite element numerical analysis [20]. Previous studies have used ANSYS to establish 3D geometric models of complex, large-scale hydropower arch dam-foundation systems and performed mesh generation for these models [21]. Additionally, 3D FEMs have been developed for the Moon, allowing the use of digital elevation models (DEM) for any location of interest to simulate significant variations in lateral heat transfer caused by topography [22]. By extracting the desired region from large DEM, a triangular irregular network can be constructed to capture the topographic surface, providing a realistic representation of terrain features [23,24]. Although the best topographic surface models are often provided through terrain entity interpretation [25] and machine learning algorithms [26], using ANSYS to build 3D terrain flow grids from DEM, while accounting for 3D terrain effects enhances the model's practical applicability [27]. In this study, DEM data are utilized to construct a 3D geological FEM. ANSYS is subsequently employed to simulate the regional geological structure of the JSS as a case study. Additionally, actual strain and tilt data from the JSS are integrated to validate the effectiveness of strain and deformation analysis based on 3D geological FEM.

2. Data

The data used in this study primarily include DEM data, regional rock mechanical parameters, and extensometer and tiltmeter observations. The DEM data are sourced from the GDEM V2 dataset available on the Geospatial Data Cloud website (www.gscloud.cn)

(accessed on 1 June 2023). The selected geographical range of the DEM data is between 29.41°N to 29.66°N and 115.86°E to 116.08°E, which is used to create a 3D digital terrain model for an area of 28 km north–south (NS) by 21.5 km east–west (EW) around the JSS. The area near the JSS is divided into different lithological blocks based on rock distribution, corresponding to varying physical and mechanical parameters of the rocks. The regional rock mechanical parameters (Table 1) are derived from the regional geological map produced by the Jiangxi Provincial Bureau of Geology and Mineral Resources. The extensometer and tiltmeter (Figure 2) observations are obtained from the deformation monitoring conducted at the JSS by the Jiangxi Earthquake Agency, with the selected data covering the period from 1 January 2011 to 31 December 2020.

Table 1. Mechanical parameters of rock.

Lithology	Slate	Limestone	Granite	Sand Soil
Bulk Density/(kg·m ^{−3})	2750	2600	2650	2200
Compressive Strength/Mpa	150	100	200	10
Young’s Modulus/Gpa	50	78	80	3.6
Poisson’s Ratio	0.25	0.32	0.29	0.22
Thermal Expansion (10 ^{−6} /°C)	8.7	7.3	7.5	5

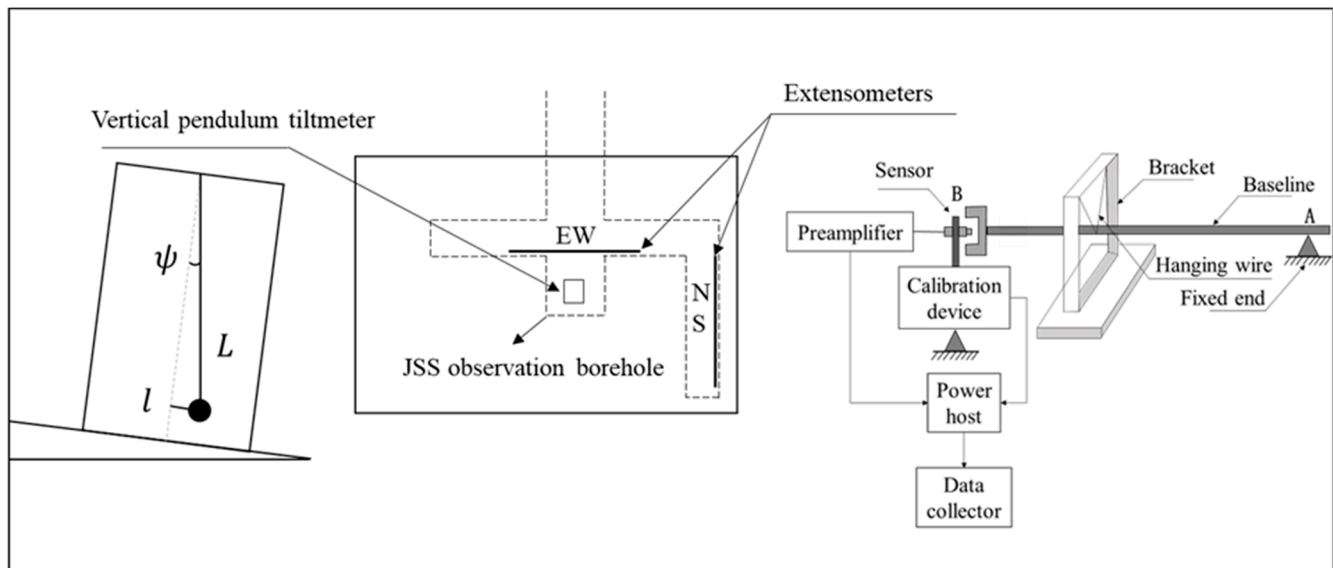


Figure 2. The extensometers and tiltmeter at JSS observation borehole. The central box represents the JSS observation borehole, with the observation principles of the extensometer on the right and the vertical pendulum tiltmeter on the left.

In Figure 2, the extensometer works by connecting the fixed end (Point A) and the support end (Point B) to the measured structure. A sensor detects the displacement between the two points. The sensor converts the mechanical displacement into an electrical signal, which is amplified by a preamplifier and transmitted to the data acquisition system. A calibration device ensures the accuracy of the measurements, while an electromagnetic mainframe powers the system. The entire device uses wires and a baseline as reference points to precisely measure the deformation of the structure under external forces, providing data for studying the pattern of horizontal strain changes during earthquake preparation. This instrument measures the relative variation in horizontal distance between two points within the crustal rock mass, from which the strain between the two points is calculated, defined as [28]:

$$\epsilon = \frac{\lambda - \lambda'}{\lambda} \quad (1)$$

where ε is the relative change in horizontal distance between two points in the crustal rock mass, λ is the original distance between two points on the surface of the crust; λ' is the distance between the two points on the surface of the crust after deformation.

Additionally, according to the measurement principle of the vertical pendulum tiltmeter in Figure 2, the pendulum is suspended from the top and hangs freely, remaining perpendicular to the ground. When the ground tilts, the pendulum, due to gravity, stays vertical, forming a tilt angle with the ground. By measuring the horizontal displacement of the pendulum and the pendulum length, the tilt angle of the ground can be calculated, allowing for monitoring of ground or structural inclination changes. Tiltmeters are fundamental instruments for studying solid tides and earthquakes, playing a crucial role in the observation and research of crustal deformation [29,30]. This instrument measures the tilt of the crust relative to the vertical (zenith) line, defined as:

$$\psi = \frac{l}{L} \rho \quad (2)$$

where l is the displacement of the pendulum relative to its own body; L is the length of the pendulum; $\rho = 206,265$ is the radian-to-arcseconds conversion coefficient; ψ is the tilt degree of the crust relative to the vertical line.

3. Model and Methods

3.1. 3D Geological FEM

Using the aforementioned DEM data, rock distribution, and regional rock mechanical parameters, a 3D geological FEM can be created around the JSS. The creation process is shown in Figure 3. First, contour lines are extracted from the DEM data of the JSS region and used to generate a 3D mesh in AutoCAD. This 3D mesh is then imported into Rhino software (version 6.9, dated 22 October 2023) to create a digital 3D topographic model. Geological rock characteristic parameters (Slate, Limestone, Granite, Sand Soil from the regional geological map produced by the Jiangxi Provincial Bureau of Geology and Mineral Resources) are then assigned to different regions, forming a comprehensive 3D geological FEM with the finite element modeling software ANSYS Workbench (version 16.0, dated 22 October 2023). The 3D geological FEM takes into account both terrain features and lithological characteristics, serving as the foundational model for finite element analysis of strain and deformation.

When constructing a 3D geological FEM using the finite element modeling software ANSYS Workbench, the following points need to be considered [31–35]:

1. Rock module division: In the Space Claim module, the 3D digital terrain model is divided into several modules based on rock distribution characteristics, and different lithological mechanical parameters are assigned to each (Table 1).
2. Finite element mesh division: The model is discretized to obtain relatively accurate solutions using discrete mesh elements, balancing computational efficiency and accuracy. If the mesh is too dense, it increases the computational load; if too sparse, it reduces result resolution. The 3D digital topographic model, based on DEM data, represents the terrain's original size (28 km NS by 21.5 km EW). Considering both computational load and accuracy, a grid size of 1 km is selected.
3. Contact relationships: When a geometry contains multiple components, the relationships between the components need to be defined, as the contact between them affects the load transfer mechanisms. Workbench provides various types of contact relationships, and it is necessary to determine the friction and cohesion coefficients between different rock layers. As no slippage occurs between the layers, this study uses bonded contact relationships to define the load transfer mode, ensuring precise interaction between layers.
4. Boundary conditions: For solving the model, loads and constraints need to be applied, primarily involving gravity loads and temperature constraints. Gravity is set using the standard Earth's gravitational constant of 9.8066 m/s^2 . The JSS region experiences

significant temperature variations, with an average monthly temperature ranging from 0 °C to 30 °C. Based on altitude affecting the temperature gradient, the model is divided into four levels, with a 3 °C temperature difference between adjacent levels, reflecting the approximately 9 °C temperature variation from the base to the summit of Lushan Mountain.

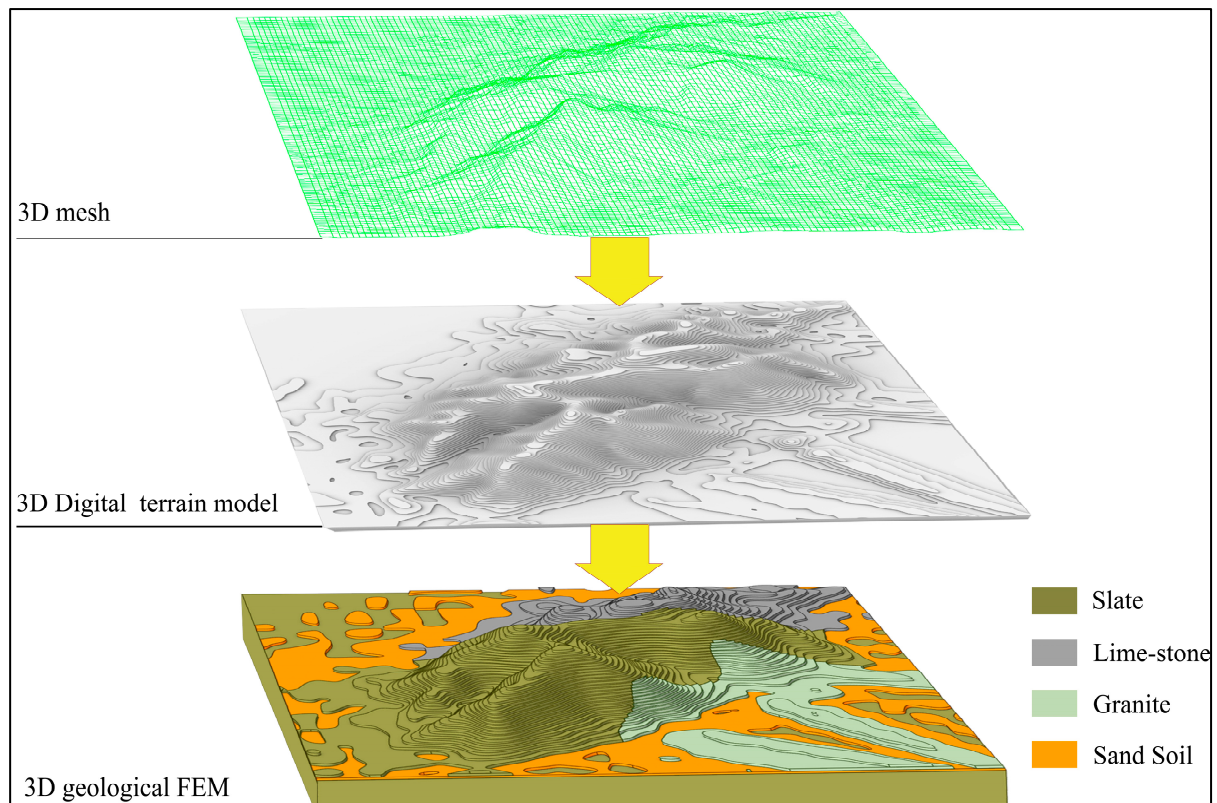


Figure 3. Generation of a regional 3D geological FEM of JSS. The top green grid represents the 3D mesh generated using DEM data, the middle gray model is the 3D digital terrain model, and the bottom colored model is the 3D geological FEM.

The 3D geological FEM constructed in this study is based on data-driven modeling, utilizing field data characteristics to build a more accurate representation of the geological conditions. The integration of high-resolution DEM data enhances the model's topographical precision, while the inclusion of rock distribution and rock mechanical parameters ensures a more reliable depiction of local geological features. During the modeling process, precise mesh generation for the target area and the application of specific boundary conditions are implemented to construct the geological entity, thereby improving the effectiveness of finite element analysis. Since its introduction in 1993, 3D geological modeling has evolved over the past three decades, with methodologies varying by region and discipline [36]. Many current studies rely on 3D numerical models constructed from contour lines [37,38], while others use lithological sample data to create solid 3D models [39,40]. More recent approaches are exploring artificial intelligence-based methods for 3D geological modeling [41,42]. In this section, the DEM is integrated with geological data to provide visual representations, utilizing one of the mainstream approaches in contemporary 3D geological modeling.

3.2. Strain and Deformation Analysis

The process of strain and deformation analysis using the 3D geological FEM is illustrated in Figure 4. First, a digital 3D terrain model is constructed using DEM data. Then, regional geological rock properties are added to establish a 3D geological FEM, simulating

regional geological structures. Next, by applying gravity loads and temperature constraints to the model, the directional strain and deformation solutions of the FEM are obtained. Finally, the calculated results of the FEM are compared to actual data from a regional seismic station to verify the feasibility of strain and deformation analysis using 3D geological FEM. This process will be demonstrated using the JSS of the Lushan Mountains (Figure 1) as an example.

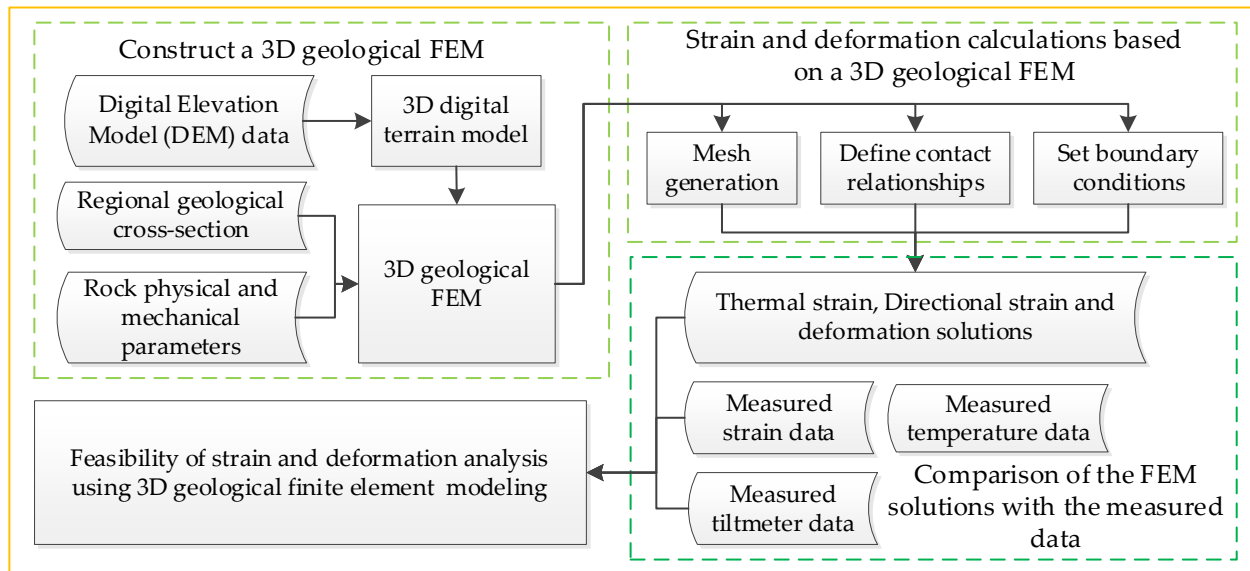


Figure 4. The process of strain and deformation analysis with 3D geological FEM.

Figure 4, the FEM is used to simulate regional strain and deformation under complex conditions, including topography, lithological distribution, and temperature variations. One-dimensional (1D) or 2D models are typically insufficient to fully capture the strain and deformation characteristics of mountainous regions. Therefore, this study establishes a 3D FEM to analyze the strain and deformation distribution. The 3D finite element equations are employed to determine the strain state at specific points within the 3D elastic body in vector form, with the six independent strain components expressed as follows [31,43]:

$$\varepsilon = \{\varepsilon\} = \begin{Bmatrix} \varepsilon_x \\ \varepsilon_y \\ \varepsilon_z \\ \gamma_{xy} \\ \gamma_{yz} \\ \gamma_{zx} \end{Bmatrix} \quad (3)$$

where x, y, z represent the three components of a 3D Cartesian coordinate system.

Additionally, in practical applications, the effect of thermal strain is one of the key factors that needs to be carefully considered. Thermal strain is caused by temperature changes, which do not yield shear strains. Therefore, the 3D thermal strain equation is as follows [31]:

$$\varepsilon_T = \begin{Bmatrix} \varepsilon_x \\ \varepsilon_y \\ \varepsilon_z \\ \gamma_{xy} \\ \gamma_{yz} \\ \gamma_{zx} \end{Bmatrix} = \begin{Bmatrix} \alpha \Delta T \\ \alpha \Delta T \\ \alpha \Delta T \\ 0 \\ 0 \\ 0 \end{Bmatrix} \quad (4)$$

where α represents the coefficient of thermal expansion, ΔT represents the change in temperature.

Total strain is given by:

$$\varepsilon = \varepsilon_e + \varepsilon_T \quad (5)$$

where ε_e is the elastic strain due to mechanical load (such as gravity or external forces).

Strain is derived from the displacement field using the strain–displacement relationship. The displacement field can be characterized as:

$$\mathbf{d} = \begin{Bmatrix} u(x, y, z) \\ v(x, y, z) \\ \omega(x, y, z) \end{Bmatrix} = \begin{Bmatrix} \sum_{i=1}^N N_i u_i \\ \sum_{i=1}^N N_i v_i \\ \sum_{i=1}^N N_i \omega_i \end{Bmatrix} \quad (6)$$

where u, v, ω represent the nodal displacement values of the element, and N denotes the number of nodes on the element. The finite element formulations involve discretizing a 3D domain into smaller elements, allowing for the approximation of complex physical behaviors by dividing the domain into manageable sub-regions and facilitating the analysis of strain and deformation within each element.

The relationship between strain and displacement can be characterized as:

$$\begin{aligned} \varepsilon_x &= \frac{\partial u}{\partial x}, \varepsilon_y = \frac{\partial v}{\partial y}, \varepsilon_z = \frac{\partial \omega}{\partial z}, \\ \gamma_{xy} &= \frac{\partial v}{\partial x} + \frac{\partial u}{\partial y}, \gamma_{yz} = \frac{\partial \omega}{\partial y} + \frac{\partial v}{\partial z}, \gamma_{xz} = \frac{\partial u}{\partial z} + \frac{\partial \omega}{\partial x} \end{aligned} \quad (7)$$

This can be simplified as:

$$\varepsilon = \mathbf{B} \mathbf{d} \quad (8)$$

where \mathbf{B} represents the matrix between the nodal displacement vector \mathbf{d} and the strain vector ε .

To describe the relationship between displacement and stress, Young's modulus E can be introduced to construct the element's stiffness matrix \mathbf{K} , expressed as:

$$\mathbf{K} = \int_v \mathbf{B}^T \mathbf{E} \mathbf{B} dv \quad (9)$$

The system must satisfy the equilibrium equations, which are expressed as follows:

$$\begin{aligned} \frac{\partial(E\varepsilon_x)}{\partial x} + \frac{\partial(E\gamma_{xy})}{\partial y} + \frac{\partial(E\gamma_{yz})}{\partial z} + f_x &= 0 \\ \frac{\partial(E\gamma_{yx})}{\partial x} + \frac{\partial(E\varepsilon_y)}{\partial y} + \frac{\partial(E\gamma_{yz})}{\partial z} + f_y &= 0 \\ \frac{\partial(E\gamma_{zx})}{\partial x} + \frac{\partial(E\gamma_{zy})}{\partial y} + \frac{\partial(E\varepsilon_z)}{\partial z} + f_z &= 0 \end{aligned} \quad (10)$$

where $\mathbf{f} = [f_x \ f_y \ f_z]$ represents the nodal force vector.

In order to obtain the strain and displacement deformation solutions, the Equations (5), (7), and (10) must be solved under the conditions set for the 3D geological FEM, which include rock module division, finite element mesh division, contact relationships, and boundary conditions. Since analytical solutions are often difficult to achieve, numerical methods such as 3D finite element analysis are commonly applied. The strain and displacement deformation obtained from solving Equations (3) to (10) under the 3D geological model conditions are then compared with the strain measured by the extensometer in Equation (1) and the deformation observed by the tiltmeter in Equation (2).

4. Results

4.1. 3D Geological FEM Strain and Deformation

The temperature in the study area is significantly influenced by the terrain elevation, with the mountain's altitude reaching 1474 m and a temperature difference of approximately 9 °C between the base and the summit. Therefore, it is necessary to first analyze the thermal strain due to temperature changes. The thermal strain analysis focuses primarily on the impact of temperature at the base of the 3D geological FEM model on strain. Subsequently, the strain and deformation solutions of the model under a specific bottom temperature condition are further analyzed.

Figure 5 shows the results of the thermal strain analysis. In the finite element thermal strain analysis, the base of the constructed 3D geological FEM model is set to four temperature conditions: 0 °C, 10 °C, 20 °C, and 30 °C, based on the monthly average temperature variation range (0 °C to 30 °C) in the study area. Additionally, the coefficient of thermal expansion is set as the thermal expansion parameter for different rock blocks in the region (Table 1). This reflects the strain differences caused by annual temperature changes in the region. Figure 5a–d respectively illustrate the thermal strain effects under the four temperature conditions set at the model's base. As the temperature increases, thermal strain grows, and the strain in the mountain also increases, placing it under tension. Conversely, as the temperature decreases, thermal strain reduces and the strain in the mountain decreases, putting it under compression. Since the temperature at the summit is lower than at the base, the thermal strain at the summit remains consistently lower than at the base.

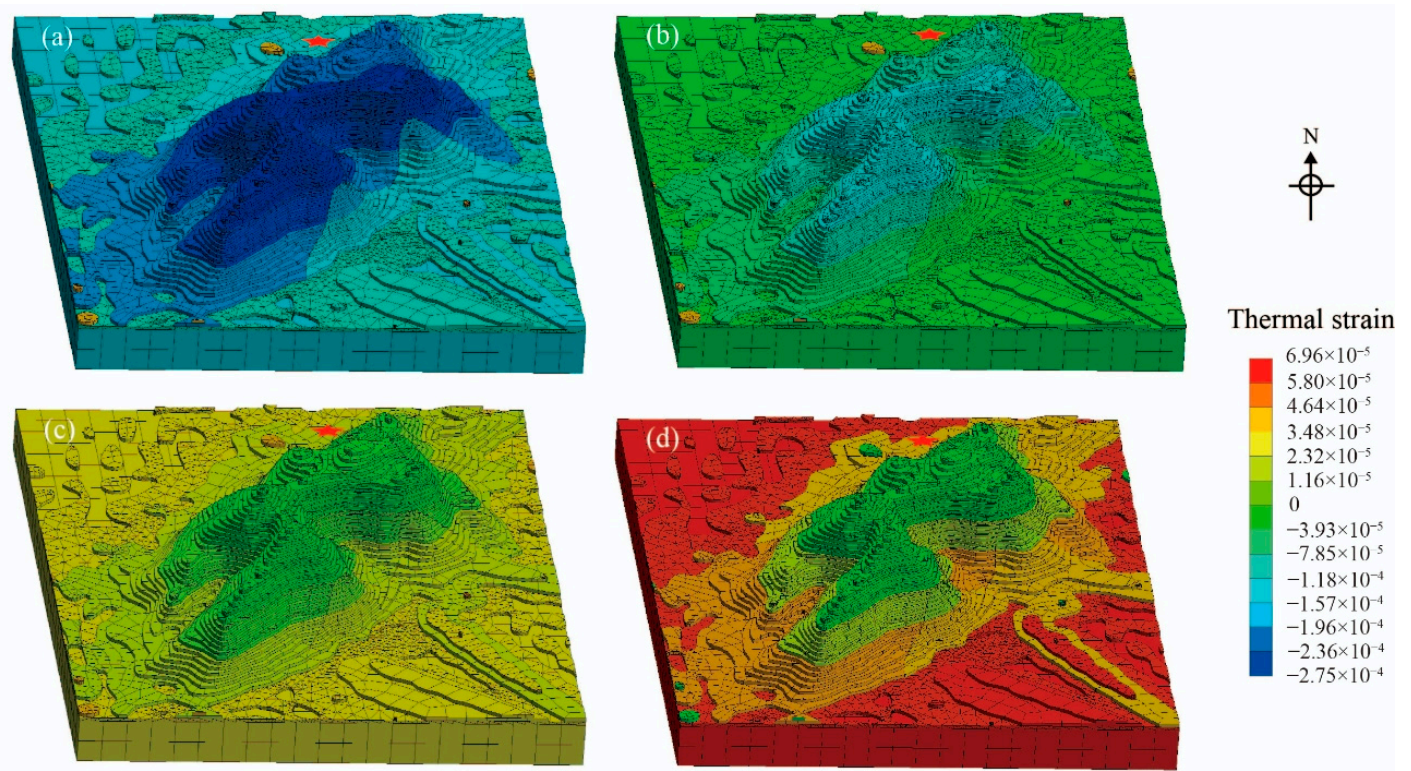


Figure 5. Thermal strain under different temperatures, with red pentagrams representing JSS. (a) Thermal strain at 0 °C; (b) thermal strain at 10 °C; (c) thermal strain at 20 °C; (d) thermal strain at 30 °C.

Figure 6 shows the strain and deformation solutions of the 3D geological FEM under the model's base temperature condition of 30 °C.

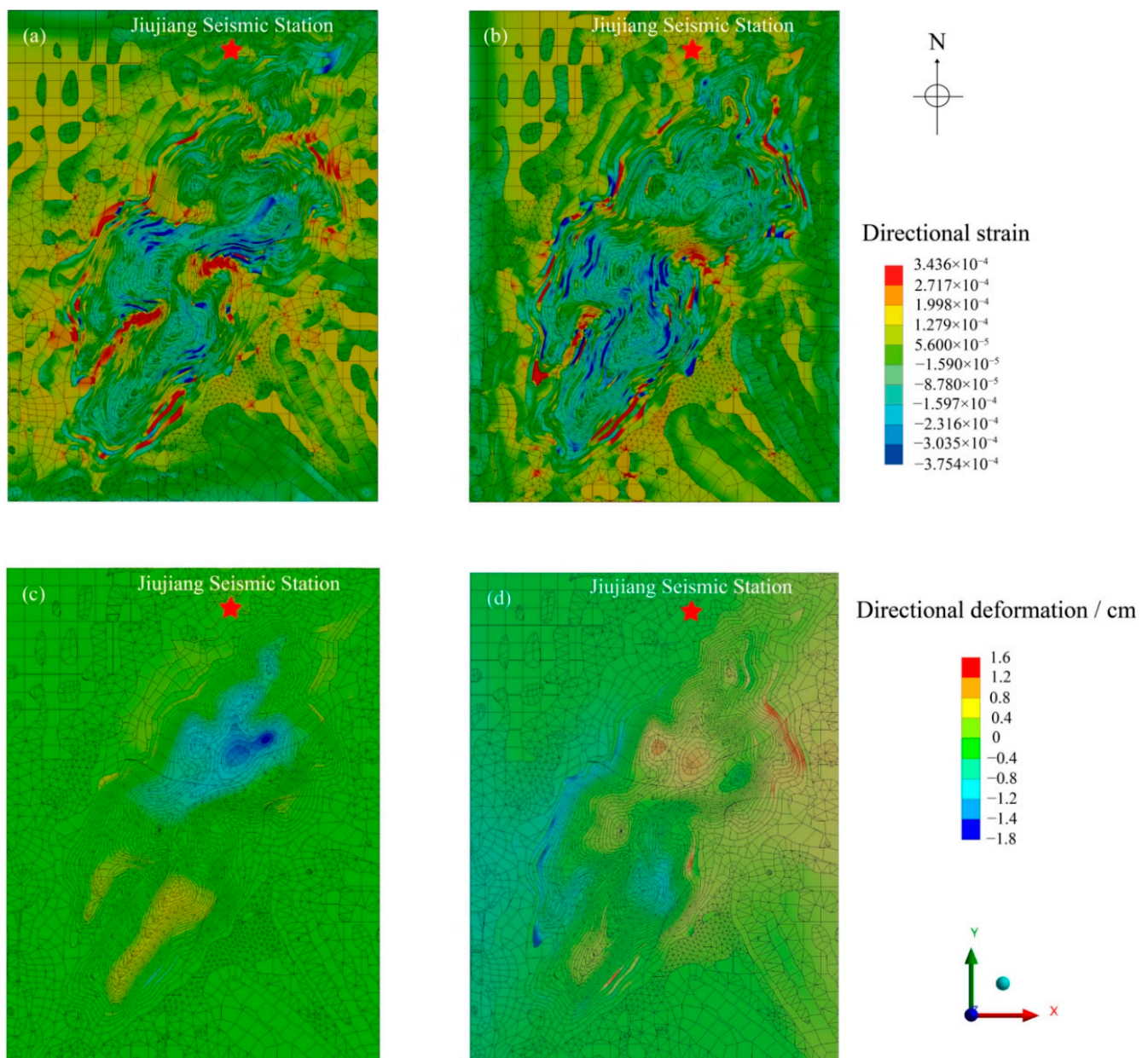


Figure 6. (a) North-South (NS) strain; (b) East-West (EW) strain; (c) NS deformation; (d) EW deformation.

Figure 6a,b display the estimated strain solutions in the north-south (NS) and east-west (EW) directions for the JSS region, respectively. The strain variation range in the study area is from -3.75×10^{-4} to 3.44×10^{-4} . Due to geological structures and temperature changes, the strain solutions vary across different locations and elevations. The maximum strain values in both NS and EW directions consistently occur at the mountain base, while the minimum values appear at the mountain summit. Since positive strain typically indicates tension and negative strain indicates compression, the stretching and compressing states across the region can be observed. Valleys tend to exhibit tensile behavior, while ridges are more prone to compression.

Figure 6c,d show the deformation solutions in the NS and EW directions, respectively. The 3D geological FEM simulates deformation magnitudes in the range of -1.8 to 1.6 cm. Influenced by factors such as gravity, temperature, topography, and geological structures, the deformation in the NS and EW directions differs significantly. In Figure 6c, the NS deformation solution is predominantly negative, indicating that the mountain exhibits a

southward tilting deformation. In Figure 6d, the EW deformation solution reveals a NE-SW extension, aligning with the general extension direction of the Lushan Mountain range. The northwestern part primarily shows negative EW deformation, while the southeastern part shows positive EW deformation, suggesting that the northwestern region tilts westward, while the southeastern region tilts eastward. Since JSS is located in the northwestern (NE) part of the study area, which experiences westward and southward deformation, it can be inferred that JSS as a whole exhibits a southwestward (SW) deformation trend.

4.2. Comparing FEM and Measured Results

To further verify the feasibility of strain and deformation analysis using 3D geological FEM, the thermal strain, directional strain, and deformation calculated from the aforementioned model are compared with the strain and deformation data measured by the extensometer and tiltmeter of the JSS over a ten-year period from 2011.0 to 2021.0. The comparison of the 3D geological FEM regional strain with the measured strain at JSS is presented in Figure 7. The comparison of the 3D geological FEM deformation with the tiltmeter observations at JSS is presented in Figure 8.

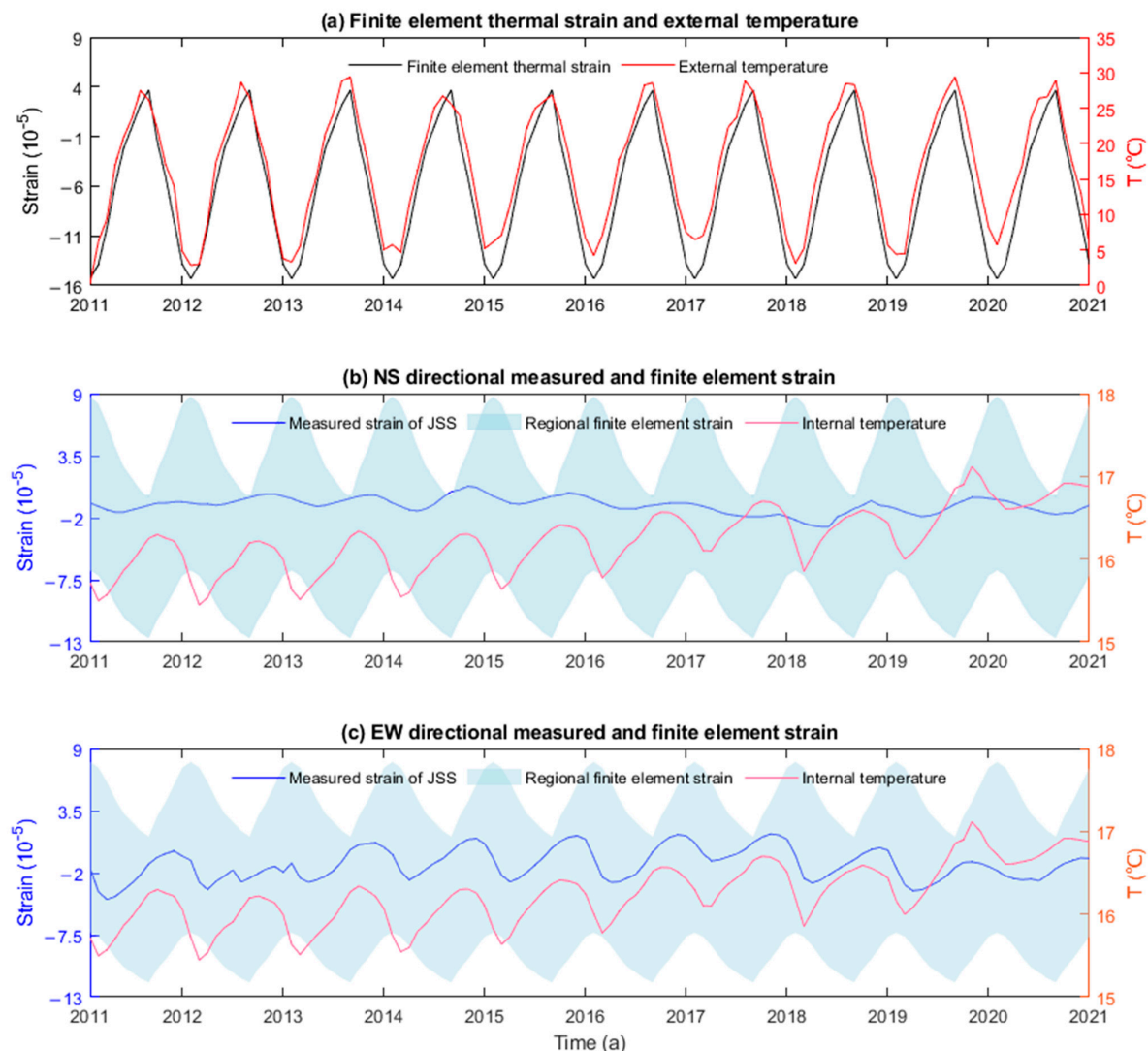


Figure 7. Comparison of the 3D geological FEM strain with the measured strain at JSS over a ten-year period from 2011.0 to 2021.0. (a) FEM thermal strain and external temperature at JSS. (b) Comparison of the NS directional regional FEM strain with the strain measured at JSS. (c) Comparison of the EW directional regional FEM strain with the strain measured at JSS. (b,c) also show the relationship between the strain and the internal temperature observed in the JSS observation tunnel.

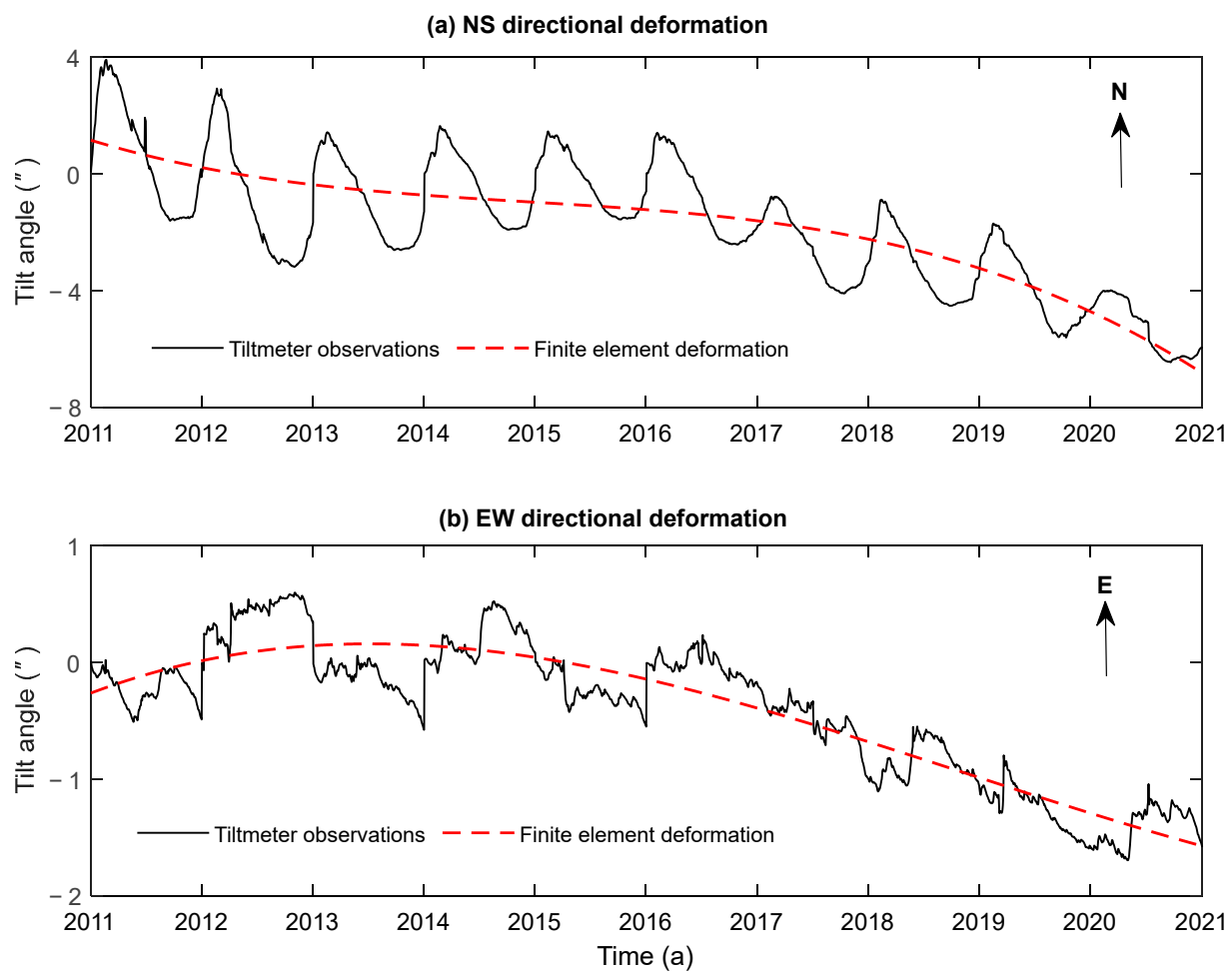


Figure 8. Comparison between the 3D geological FEM deformation model and tiltmeter observations. (a) NS directional deformation, with arrows indicating the northward direction; (b) EW directional deformation, with arrows indicating the eastward direction. The magnitude of deformation is represented by the tilt angle.

In Figure 7a, the thermal strain corresponding to each month's temperature is calculated. Using external temperature measurements obtained from the JSS, a uniform temperature processing method is applied to extract a single temperature value for each month. The results show a strong relationship between temperature and strain, with a correlation exceeding 98.7% between the measured external temperature and the thermal strain predicted by the 3D geological FEM. The regional strain calculated by the 3D geological FEM, the strain measured at JSS, and the internally measured temperature within the observation cavity at JSS in both the NS and EW directions are presented in Figure 7b,c. The FEM strain results represent the strain at each point within the regional model, leading to the use of the regional FEM strain interval. The measured strain at JSS falls within this interval of the FEM strain.

Additionally, the correlation coefficients between the internal temperature measured at JSS and the measured strain in the NS (Figure 7b) and EW (Figure 7c) directions are 0.7 and 0.85, respectively. The inconsistency in heat conduction from the external surface of the mountain to the observation cave leads to a 2–3 months phase difference between the external and internal temperature variations observed by JSS. Therefore, by shifting the FEM thermal strain time series backward by three months, the correlation between the thermal strain and the measured strain is recalculated. The correlation coefficients between the JSS measured strain and the FEM thermal strain, shifted by three months, are 0.6 in the NS direction and 0.75 in the EW direction. The measured strain at JSS aligns with the

range of FEM strain, and the strong correlation between the JSS measurements and the FEM thermal strain indicates that the FEM strain accurately reflects the magnitude of the measured strain within a certain range, demonstrating a close relationship between FEM strain and the measured strain.

Figure 8 presents the deformation data in the NS and EW directions, respectively. The deformation data are derived from the 3D geological FEM results and tiltmeter observations. As shown in Figure 8a, the annual variation trend of the observed NS directional deformation indicates a tilt toward the south. Similarly, Figure 8b demonstrates that the annual variation trend of the observed EW directional deformation indicates a tilt toward the west. The annual deformation trend observed by the JSS tiltmeter shows an overall tilt toward the southwest, which is consistent with the results of the 3D geological FEM. The correlation coefficient between the deformation observed by the JSS tiltmeter and the FEM simulation is 0.8 in the NS direction and 0.9 in the EW direction, suggesting that the deformation results from the 3D geological FEM can reasonably represent the actual tilting observed by the JSS to some extent.

5. Discussion

This study conducts strain and deformation analysis using a 3D FEM, considering factors such as topography, geological structures, gravity, and temperature. In real deformation processes, changes in groundwater and rainfall significantly influence crustal deformation, especially in areas with marked variations in rock pore pressure [36]. The infiltration of precipitation and fluctuations in groundwater levels can alter local stress conditions, leading to surface deformation. Therefore, integrating hydrological parameters with the 3D geological FEM helps provide a more comprehensive understanding of groundwater flow's role in crustal strain and deformation. Additionally, rock mechanical properties are key parameters in FEM modeling. Using more detailed rock distribution and parameter settings—such as Young's modulus, Poisson's ratio, and fracture toughness—can enable more precise calibration of FEM. Variations in the elastic properties of different rock types can lead to significant differences in how strain accumulates and releases under external forces [44,45]. Furthermore, the nonlinear behavior of rock materials caused by seismic events, such as fault slip, stress concentration, and fracturing, must be considered [46]. These behaviors cannot be captured by purely linear elastic FEMs [47–49]. Incorporating nonlinear mechanical behavior models and considering plastic deformation or damage mechanics will enhance FEM's ability to predict strain during and after seismic events. Future research will attempt to introduce other factors affecting strain and deformation, such as hydrological conditions, seismic activity, or the nonlinear mechanical behavior of rock masses. By coupling multiple physical fields into existing geological FEMs, stress and strain variations in real environments can be more accurately simulated, providing a more comprehensive theoretical basis for predicting geological disasters.

Although 3D geological FEM can offer strain and deformation analysis, the application of a single model has limitations. Integrating FEM with other monitoring technologies could improve the monitoring accuracy and coverage of regional crustal deformation. For instance, combining interferometric synthetic aperture radar (InSAR) with FEM provides a comprehensive framework for both large-scale and detailed analyses [50,51]. InSAR offers macroscopic observational data of surface deformation, while FEM allows detailed stress and deformation analysis for localized areas. This combination can improve overall model prediction accuracy, particularly in areas with uneven strain distribution. In regions with sparse GNSS stations, interpolating and extending GNSS data can offer more detailed stress and deformation distribution maps [52,53]. Additionally, GNSS provides high temporal resolution real-time monitoring data, which can be used to update FEM models in real-time, significantly enhancing their predictive capability. For example, post-earthquake GNSS-observed deformation can be used to immediately correct and update FEM. In 3D geological FEM, real-time monitoring data (such as GNSS, InSAR, or inclinometer data) can be assimilated into the model, continuously updating its state and parameters.

This allows the model to optimize over time and improve its predictive ability. Real-time data assimilation can significantly enhance FEM's application in dynamic environments, especially for emergency response during seismic activity.

Through model optimization and multi-source data fusion, FEM models will be better equipped to capture dynamic changes in regional crustal strain and deformation, aligning more closely with actual observational data and further enhancing the model's reliability and predictive capability. Future studies that incorporate these optimization methods will enable more accurate and comprehensive research, providing stronger technical support for regional crustal deformation monitoring.

6. Conclusions

Using regional geological and terrain structure data of Lushan Mountain, the ANSYS Workbench module is employed to establish a 3D geological FEM to validate the feasibility of this approach for regional strain and deformation analysis. The method first constructs a digital 3D terrain model from DEM data, then integrates regional geological rock mass properties to develop a 3D geological FEM that simulates regional geological structures. Gravity load and thermal constraints are applied to derive the directional strain and deformation solutions using the finite element method. Based on the calculations of directional strain and deformation from the 3D geological FEM, in conjunction with strain and tilt data measured by the JSS, the results lead to the following conclusions:

1. The 3D geological FEM thermal strain analysis reveals that temperature variations significantly impact strain and deformation in the study area, especially due to the elevation difference between the base and summit of the mountain. As temperature increases, the thermal strain grows, leading to tensile strain in the mountain, while decreasing temperatures result in reduced thermal strain and compressive effects. The analysis shows that thermal strain is consistently lower at the summit compared to the base, reflecting the lower temperatures at higher altitudes. This indicates that the terrain's elevation plays a critical role in influencing the strain distribution due to temperature changes, with the base experiencing greater thermal expansion effects.
2. The results of strain and deformation analysis using the 3D geological FEM indicate significant variations in strain and deformation across the study area due to factors such as temperature, geological structures, gravity, and topography. The strain variation range is from -3.75×10^{-4} to 3.44×10^{-4} , and the deformation magnitudes in the range of -1.8 to 1.6 cm in the study area. The maximum strain values occur at the mountain base, while the minimum values are observed at the summit. Valleys generally experience tensile strain, whereas ridges undergo compression. In terms of deformation, the model shows an overall southwestward deformation in the study area.
3. The comparison of strain and deformation data from the 3D geological FEM with the measured strain and tiltmeter observations at JSS over a ten-year period demonstrates a strong consistency between the model predictions and actual measurements. The correlation coefficients between the JSS measured strain and the FEM thermal strain, adjusted by a three-month shift due to the inconsistency in heat conduction from the external surface of the mountain to the JSS observation cavity, are 0.6 in the NS direction and 0.75 in the EW direction. Additionally, the FEM accurately captures the annual deformation trends in the NS and EW directions, showing a tilt toward the southwest, which aligns with the observed deformation trends at JSS. Correlation coefficients of 0.8 in the NS direction and 0.9 in the EW direction suggest that the FEM deformation results reasonably reflect the actual deformation observed by the tiltmeter to a certain extent. The strong correlation between FEM predictions and measured data confirms the effectiveness of using 3D geological FEM for strain and deformation analysis in the region, offering valuable insights into the strain and deformation behavior of the Lushan Mountain area.

By employing finite element modeling, as demonstrated by the JSS, regions with sparse GNSS data can still effectively analyze and monitor strain and deformation. The integration of finite element modeling with digital strain and tiltmeter observations provides an alternative approach to enhancing the understanding of strain and deformation in areas where traditional GNSS-based methods are limited or insufficient. This study's methodological approach is not only effective for the JSS but also applicable to other regions with limited GNSS monitoring stations and inadequate measurement coverage, presenting a viable option for regional crustal deformation analysis.

Author Contributions: Conceptualization, M.L. and A.Z.; methodology, M.L.; software, H.L.; validation, M.L., H.L., A.E.-M., T.L. and A.Z.; formal analysis, H.L.; investigation, T.L.; resources, A.Z.; data curation, A.Z.; writing—original draft preparation, M.L.; writing—review and editing, M.L., H.L., A.E.-M., T.L. and A.Z.; visualization, H.L.; supervision, A.E.-M., T.L. and A.Z.; project administration, M.L.; funding acquisition, M.L. and T.L. All authors have read and agreed to the published version of the manuscript.

Funding: This research was funded by the National Natural Science Foundation of China (41704031, 42374040); the Natural Science Foundation of Jiangxi Science and Technology Department (20232BAB203073); the Key Laboratory of Mine Environmental Monitoring and Improving around Poyang Lake, Ministry of Natural Resources (MEMI-2021-2022-29).

Data Availability Statement: The digital elevation model (DEM) data used in this study are sourced from the GDEM V2 dataset, which is publicly available on the Geospatial Data Cloud website (www.gscloud.cn, accessed on 1 June 2023). The extensometer and tiltmeter data used for deformation monitoring were collected at the Jiangxi Seismic Station (JSS) by the Jiangxi Earthquake Agency. These datasets are available upon reasonable request from the Jiangxi Earthquake Agency, subject to relevant data sharing policies.

Acknowledgments: We would like to express our sincere gratitude to the Jiangxi Earthquake Agency for providing the observed data and related materials.

Conflicts of Interest: The authors declare no competing financial interests or personal relationships that could have appeared to influence the work reported in this paper. However, the author affiliated with Jiangxi Spatial Geographic Information Engineering Group Co., Ltd. is an employee of a commercial entity, which may benefit from the findings of this research. This does not alter the authors' adherence to all ethical standards of scientific publishing as outlined by MDPI.

References

- Andersson, J.B.H.; Bauer, T.E.; Lynch, E.P. Evolution of structures and hydrothermal alteration in a Palaeoproterozoic supracrustal belt: Constraining paired deformation-fluid flow events in an Fe and Cu-Au prospective terrain in northern Sweden. *Solid Earth* **2020**, *11*, 547–578. [\[CrossRef\]](#)
- Hamdi, L.; Defaflia, N.; Merghadi, A.; Fehdi, C.; Yunus, A.P.; Dou, J.; Pham, Q.B.; Abdo, H.G.; Almohamad, H.; Al-Mutiry, M. Ground Surface Deformation Analysis Integrating InSAR and GPS Data in the Karstic Terrain of Cheria Basin, Algeria. *Remote Sens.* **2023**, *15*, 1486. [\[CrossRef\]](#)
- Calais, E.; Camelbeeck, T.; Stein, S.; Liu, M.; Craig, T.J. A new paradigm for large earthquakes in stable continental plate interiors. *Geophys. Res. Lett.* **2016**, *43*, 10621–10637. [\[CrossRef\]](#)
- Zaccagnino, D.; Doglioni, C. Earth's gradients as the engine of plate tectonics and earthquakes. *La Riv. Nuovo C.* **2022**, *45*, 801–881. [\[CrossRef\]](#)
- Sun, W.K.; Zhou, X. Advances, Problems and Prospects of Modern Geodesy Applied in Tibetan Geodynamic Changes. *Acta Geol. Sin.-Engl. Ed.* **2013**, *87*, 318–332. [\[CrossRef\]](#)
- Wu, J.C.; Song, X.Y.; Wu, W.W.; Meng, G.J.; Ren, Y.Y. Analysis of Crustal Movement and Deformation in Mainland China Based on CMONOC Baseline Time Series. *Remote Sens.* **2021**, *13*, 2481. [\[CrossRef\]](#)
- Dumka, R.K.; SuriBabu, D.; Kotlia, B.S.; Kothiyari, G.C.; Prajapati, S. Crustal deformation measurements by global positioning system (GPS) along NSL, western India. *J. Geod. Geodyn.* **2022**, *13*, 254–260. [\[CrossRef\]](#)
- Li, W.G.; Ivan, I.; Liu, Y.L.; Yang, L.B. Visual Processing and Analysis of Landslide Deformation Based on GNSS. *IEEE Sens. J.* **2021**, *21*, 25260–25266. [\[CrossRef\]](#)
- Li, R.X.; Li, Z.S.; Han, J.P.; Lu, P.; Qiao, G.; Meng, X.L.; Hao, T.; Zhou, F.J. Monitoring surface deformation of permafrost in Wudaoliang Region, Qinghai-Tibet Plateau with ENVISAT ASAR data. *Int. J. Appl. Earth Obs.* **2021**, *104*, 102527. [\[CrossRef\]](#)
- Wang, Z.T.; Zhang, H.; Meng, Q.; Shi, Y.L. Finite element simulation of deformation and stress changes of Kalpin-Kemin fault system in the Southwest Tianshan Orogenic Belt. *Sci. China Earth Sci.* **2022**, *65*, 863–873. [\[CrossRef\]](#)

11. Dyksterhuis, S.; Albert, R.A.; Müller, R.D. Finite-element modelling of contemporary and palaeo-intraplate stress using ABAQUS™. *Comput. Geosci.* **2005**, *31*, 297–307. [\[CrossRef\]](#)
12. Yadav, R.; Tiwari, V.M. Numerical simulation of present day tectonic stress across the Indian subcontinent. *Int. J. Earth Sci.* **2018**, *107*, 2449–2462. [\[CrossRef\]](#)
13. Singh, S.; Ghosh, A. The role of crustal models in the dynamics of the India-Eurasia collision zone. *Geophys. J. Int.* **2020**, *223*, 111–131. [\[CrossRef\]](#)
14. Deng, Z.; Hu, M.Q.; Zhou, B.; Lu, Y.Z.; Tao, T.L.; Ma, X.J.; Jiang, H.; Li, H. Preliminary study on application of numerical simulation methods to earthquake prediction research (II). *Dizhen Dizhi* **2011**, *33*, 670–683. [\[CrossRef\]](#)
15. Lobatskaya, R.M.; Strelchenko, I.P.; Dolgikh, E.S. Finite-element 3D modeling of stress patterns around a dipping fault. *Geosci. Front.* **2018**, *9*, 1555–1563. [\[CrossRef\]](#)
16. Ofoegbu, G.I.; Ferrill, D.A.; Smart, K.J.; Stamatakos, J.A. Uncertainties in earthquake magnitudes from surface fault displacement based on finite element modeling. *Int. J. Rock Mech. Min. Sci.* **1997**, *34*, e231–e233. [\[CrossRef\]](#)
17. Zhu, A.Y.; Zhang, D.N.; Guo, Y.X. The numerical simulation on the seismogenic mechanism of the Lushan 7.0 earthquake constrained by deformation observation. *Chin. J. Geophys.* **2016**, *59*, 1661–1672. [\[CrossRef\]](#)
18. Sadeghi-Farshbaf, P.; Khatib, M.M.; Nazari, H. Future stress accumulation zones around the main active faults by 3D numerical simulation in East Azerbaijan Province, Iran. *Acta Geod. Geophys.* **2019**, *54*, 461–481. [\[CrossRef\]](#)
19. Zhu, A.; Zhang, D.; Jiang, C. Numerical simulation of the relationship between the tectonic stress distribution and the historical strong earthquake activities of the middle-southern segment of eastern boundary of the Sichuan-Yunnan block. *Acta Seismol. Sin.* **2015**, *37*, 762–773. [\[CrossRef\]](#)
20. Long, S.; He, T.; Liang, Q.; Lan, K.; Lin, J.; Dong, Y.; He, J. A High Precision Automatic 3D Geological Modeling Method Based on ANSYS Workbench: A Case Study of Gas Hydrate-related Slipstream Submarine Slide. *Beijing Daxue Xuebao (Ziran Kexue Ban)/Acta Sci. Nat. Univ. Pekin.* **2018**, *54*, 994–1002. [\[CrossRef\]](#)
21. Zhou, H.; Wu, X.T.; Zhou, D.N.; Tian, T. A Coupling Modeling Method with ANSYS/FLAC and Its Application. *Appl. Mech. Mater.* **2012**, *170–173*, 3402–3405. [\[CrossRef\]](#)
22. Prasad, K.D.; Rai, V.K.; Murty, S.V.S. A Comprehensive 3D Thermophysical Model of the Lunar Surface. *Earth Space Sci.* **2022**, *9*, e2021EA001968. [\[CrossRef\]](#)
23. Bilal, M.; Sridhar, N.; Araya, G.; Parameswaran, S.; Birkelund, Y. Wind Flow over a Complex Terrain in Nygardsfjell, Norway. In Proceedings of the Asme 9th International Conference on Energy Sustainability, San Diego, CA, USA, 28 June–2 July 2015. [\[CrossRef\]](#)
24. López, E.C.; Casino, E.S.; Escibano, J.F.; Ureña, A.V. Application of Finite Element Method to Create a Digital Elevation Model. *Mathematics* **2023**, *11*, 1522. [\[CrossRef\]](#)
25. Sun, W.; Wang, H.; Zhao, X. A simplification method for grid-based DEM using topological hierarchies. *Surv. Rev.* **2018**, *50*, 454–467. [\[CrossRef\]](#)
26. Alzaghouli, E.; Al-Zoubi, M.B.; Obiedat, R.; Alzaghouli, F. Applying Machine Learning to DEM Raster Images. *Technologies* **2021**, *9*, 87. [\[CrossRef\]](#)
27. Zhang, R.; Wang, X.L. Numerical Simulation for 3-D Wind Fields in Suburban Environment with Topographic Effects. In Proceedings of the Asme International Mechanical Engineering Congress and Exposition, Houston, TX, USA, 13–19 November 2015. [\[CrossRef\]](#)
28. Hashiguchi, K.; Yamakawa, Y. *Introduction to Finite Strain Theory for Continuum Elasto-Plasticity*; Wiley: Hoboken, NJ, USA, 2013. [\[CrossRef\]](#)
29. Xia, J.N.; Lin, Q.; Geng, L.X.; Li, Z.; Luo, S.; Li, N.F.; Yu, J.F.; Liu, J. Portable vertical pendulum tiltmeter development and application test. *Acta Geod. Geophys.* **2019**, *54*, 287–300. [\[CrossRef\]](#)
30. Xu, X.; Chen, Z.; Li, H.; Ma, S.G.; Wu, L.H.; Wang, W.B.; Dong, Y.K.; Zhan, W.W. Design of A High-Precision Component-Type Vertical Pendulum Tiltmeter Based on FPGA. *Sensors* **2023**, *23*, 7998. [\[CrossRef\]](#)
31. Chen, X.; Liu, Y. *Finite Element Modeling and Simulation with ANSYS Workbench*, 2nd ed.; CRC Press/Taylor and Francis: Boca Raton, FL, USA, 2018. [\[CrossRef\]](#)
32. Farshbaf, P.S.; Khatib, M.M.; Nazari, H. Solid meshing of 3D geological model in finite element analysis: A case study of East Azerbaijan, NW Iran. *Model. Earth Syst. Environ.* **2016**, *2*, 12. [\[CrossRef\]](#)
33. Gautam, P.; Verma, A.; Jha, M.; Sharma, P.; Singh, T. Effect of high temperature on physical and mechanical properties of Jalore granite. *J. Appl. Geophys.* **2018**, *159*, 460–474. [\[CrossRef\]](#)
34. Liwen, G.; Zhihui, D.; Lijuan, C.; Xing, Y.; Weiying, G. Analyses of finite element model based on station's tectonic environment: Taking Qianjiang station for example. *Acta Seismol. Sin.* **2019**, *41*, 80–91. [\[CrossRef\]](#)
35. Mavko, G.; Mukerji, T.; Dvorkin, J. *The Rock Physics Handbook: Tools for Seismic Analysis of Porous Media*, 2nd ed.; Cambridge University Press & Assessment: Cambridge, UK, 2010. [\[CrossRef\]](#)
36. Cao, X.Q.; Liu, Z.M.; Hu, C.L.; Song, X.L.; Quay, J.A.; Lu, N. Three-Dimensional Geological Modelling in Earth Science Research: An In-Depth Review and Perspective Analysis. *Minerals* **2024**, *14*, 686. [\[CrossRef\]](#)
37. Bi, L.; Liu, X.; Chen, X.; Zhu, Z. An automatic 3D modeling method based on orebody contours. *Geomat. Inf. Sci. Wuhan Univ.* **2016**, *41*, 1359–1365. [\[CrossRef\]](#)

38. Bonin, O.; Rousseaux, F. Digital Terrain Model Computation from Contour Lines: How to Derive Quality Information from Artifact Analysis. *GeoInformatica* **2005**, *9*, 253–268. [\[CrossRef\]](#)
39. Zhou, F.; Li, M.; Huang, C.; Liang, H.; Liu, Y.; Zhang, J.; Wang, B.; Hao, M. Lithology-Based 3D Modeling of Urban Geological Attributes and Their Engineering Application: A Case Study of Guang'an City, SW China. *Front. Earth Sci.* **2022**, *10*, 918285. [\[CrossRef\]](#)
40. Liu, X.-Y.; Li, A.; Chen, H.; Men, Y.-Q.; Huang, Y.-L. 3D Modeling Method for Dome Structure Using Digital Geological Map and DEM. *ISPRS Int. J. Geo-Inf.* **2022**, *11*, 339. [\[CrossRef\]](#)
41. Mendoza Veirana, G.M.; Perdomo, S.; Ainchil, J. Three-dimensional modelling using spatial regression machine learning and hydrogeological basement VES. *Comput. Geosci.* **2021**, *156*, 104907. [\[CrossRef\]](#)
42. Jia, R.; Lv, Y.; Wang, G.; Carranza, E.; Chen, Y.; Wei, C.; Zhang, Z. A stacking methodology of machine learning for 3D geological modeling with geological-geophysical datasets, Laochang Sn camp, Gejiu (China). *Comput. Geosci.* **2021**, *151*, 104754. [\[CrossRef\]](#)
43. Ren, S.; Liu, H.; Song, C.; Li, J.; Yang, F.; Wang, W.; Huang, P. Metamorphism and Deformation of the Lushan Metamorphic Core Complex and Their Tectonic Significance. *Geol. Rev.* **2015**, *61*, 752–766. [\[CrossRef\]](#)
44. Małkowski, P.; Niedbalski, Z.; Balarabe, T. A statistical analysis of geomechanical data and its effect on rock mass numerical modeling: A case study. *Int. J. Coal Sci. Technol.* **2021**, *8*, 312–323. [\[CrossRef\]](#)
45. Jing, L. A review of techniques, advances and outstanding issues in numerical modelling for rock mechanics and rock engineering. *Int. J. Rock Mech. Min. Sci.* **2003**, *40*, 283–353. [\[CrossRef\]](#)
46. Guo, P.; Yao, L.H.; Ren, D.S. Simulation of three-dimensional tectonic stress fields and quantitative prediction of tectonic fracture within the Damintun Depression, Liaohe Basin, northeast China. *J. Struct. Geol.* **2016**, *86*, 211–223. [\[CrossRef\]](#)
47. Chen, Y.X.; Yang, H.X.; Ye, Y.C.; Li, J.Y. Generation of 3D finite element mesh of layered geological bodies in intersecting fault zones. *PLoS ONE* **2024**, *19*, e0293193. [\[CrossRef\]](#) [\[PubMed\]](#)
48. Feng, J.W.; Shang, L.; Li, X.Z.; Luo, P. 3D numerical simulation of heterogeneous in situ stress field in low-permeability reservoirs. *Petrol. Sci.* **2019**, *16*, 939–955. [\[CrossRef\]](#)
49. Markou, N.; Papanastasiou, P. 3D Geomechanical Finite Element Analysis for a Deepwater Faulted Reservoir in the Eastern Mediterranean. *Rock. Mech. Rock. Eng.* **2024**, 1–22. [\[CrossRef\]](#)
50. Chen, Y.; Xia, J.S.; Yu, C.; Chen, B.Q. Editorial: InSAR crustal deformation monitoring, modeling and error analysis. *Front. Environ. Sci.* **2022**, *10*. [\[CrossRef\]](#)
51. Tondas, D.; Ilieva, M.; van Leijen, F.; van der Marel, H.; Rohm, W. Kalman filter-based integration of GNSS and InSAR observations for local nonlinear strong deformations. *J. Geodesy* **2023**, *97*, 109. [\[CrossRef\]](#)
52. Bian, W.W.; Wu, J.C.; Wu, W.W. Recent Crustal Deformation Based on Interpolation of GNSS Velocity in Continental China. *Remote Sens.* **2020**, *12*, 3753. [\[CrossRef\]](#)
53. Li, Z.; Lu, T.D.; Yu, K.G.; Wang, J. Interpolation of GNSS Position Time Series Using GBDT, XGBoost, and RF Machine Learning Algorithms and Models Error Analysis. *Remote Sens.* **2023**, *15*, 4374. [\[CrossRef\]](#)

Disclaimer/Publisher's Note: The statements, opinions and data contained in all publications are solely those of the individual author(s) and contributor(s) and not of MDPI and/or the editor(s). MDPI and/or the editor(s) disclaim responsibility for any injury to people or property resulting from any ideas, methods, instructions or products referred to in the content.